Cellular Exchange Imaging (CEXI): Evaluation of a diffusion model including water exchange in cells using numerical phantoms of permeable spheres

Rémy Gardier[1] | **Juan Luis Villarreal Haro[1]** | **Erick J. Canales-Rodríguez[1]** |
Ileana O. Jelescu[2,3] | **Gabriel Girard[1,4]** | **Jonathan Rafael-Patiño[1,2]** |
Jean-Philippe Thiran[1,2,5]

[1]Signal Processing Laboratory (LTS5), École Polytechnique Fédérale de Lausanne (EPFL), Lausanne, Switzerland

[2]Radiology Department, Centre Hospitalier Universitaire Vaudois (CHUV) and University of Lausanne (UNIL) (CHUV-UNIL), Lausanne, Switzerland

[3]School of Biology and Medicine, University of Lausanne (UNIL), Lausanne, Switzerland

[4]Department of Computer Science, Université de Sherbrooke, Sherbrooke, Canada

[5]CIBM Center for Biomedical Imaging, Lausanne, Switzerland

Correspondence
Rémy Gardier, Signal Processing Laboratory (LTS5), Station 11, 1015 Lausanne, Switzerland.
Email: remy.gardier@epfl.ch

Funding information
Schweizerischer Nationalfonds zur Förderung der Wissenschaftlichen Forschung, Grant/Award Numbers: 205320_175974, 205320_204097, PZ00P2_185814

Purpose: Biophysical models of diffusion MRI have been developed to characterize microstructure in various tissues, but existing models are not suitable for tissue composed of permeable spherical cells. In this study we introduce Cellular Exchange Imaging (CEXI), a model tailored for permeable spherical cells, and compares its performance to a related Ball & Sphere (BS) model that neglects permeability.

Methods: We generated DW-MRI signals using Monte-Carlo simulations with a PGSE sequence in numerical substrates made of spherical cells and their extracellular space for a range of membrane permeability. From these signals, the properties of the substrates were inferred using both BS and CEXI models.

Results: CEXI outperformed the impermeable model by providing more stable estimates cell size and intracellular volume fraction that were diffusion time-independent. Notably, CEXI accurately estimated the exchange time for low to moderate permeability levels previously reported in other studies ($\kappa < 25$ μm/s). However, in highly permeable substrates ($\kappa = 50$ μm/s), the estimated parameters were less stable, particularly the diffusion coefficients.

Conclusion: This study highlights the importance of modeling the exchange time to accurately quantify microstructure properties in permeable cellular substrates. Future studies should evaluate CEXI in clinical applications such as lymph nodes, investigate exchange time as a potential biomarker of tumor severity, and develop more appropriate tissue models that account for anisotropic diffusion and highly permeable membranes.

KEYWORDS
compartmentalized model, diffusion MRI, exchange, lymph node, Monte-Carlo simulations, tumor microstructure

1 | INTRODUCTION

Over the last decades, diffusion-weighted magnetic resonance imaging (DW-MRI) has been used to characterize tissue microstructure, particularly with biophysical models of healthy white matter,[1-7] healthy gray matter[8-10] and tumors.[11-15] These models group the biological entities into compartments with similar contributions to the diffusion signal and differ essentially by the number of geometric features, compartments, and the targeted microstructure features.

One of the challenges of biophysical models is their specificity to one particular tissue, which requires rethinking the optimal model and assumptions that best capture its features. For example, blood displacement inside the tumor vessels[16-19] induces anisotropic diffusion, which usually is not accounted for in the healthy white matter.

An important assumption of most biophysical models is negligible water exchange between compartments, which might not be valid in unmyelinated tissue,[9,20,21] urging for specific models that include the water exchange between the intracellular and extracellular compartments, for example to model gray matter[9,10] or cancerous tissue.[11,22-24] The biophysical models that neglect the effect of water exchange on the signal employ acquisition sequences with short diffusion time,[8,11,16,25] while the ones that account for exchange either use non-Pulsed Gradient Spin Echo (PGSE) gradient sequences[13,14,24,26] or are based on the Kärger model of exchange.[9,10,12,27,28]

During the development of complex tissue models, their evaluation and validation in controlled environments helps identifying the best microstructure model and designing the optimal DW-MRI acquisition protocol. In this context, Monte-Carlo Diffusion Simulations (MCDS)[29-32] can be used to simulate the diffusion signals in complex substrates with known ground truth and without assuming an analytical equation, thus eliminating the comparison bias across different models. Moreover, realistic substrates[29,33-36] can be designed to study various microstructure parameters, including the membrane permeability,[30] in a controlled manner.

In this work, the performances of compartment models excluding and including water exchange between compartments were studied employing MCDS in packed spheres with finite membrane permeability. More specifically, the work focused on the influence of nonnegligible membrane permeability on microstructure estimation (i.e., the cell sizes, extracellular and intracellular diffusion coefficients and volume fractions) with a two-compartment model neglecting exchange terms (Impermeable Ball & Sphere[37]) and a newly proposed Cellular Exchange Imaging (CEXI) model that accounts for exchange (Permeable Ball & Sphere).

2 | METHODS

Employing MCDS in numerical substrates with water exchange across cell membranes, we investigated the effects of permeability on microstructure estimation by compartment-based models. Section 2.1 details the simulation framework, the choice of the simulation parameters, and the numerical substrate. Next, Section 2.2 compares the diffusion regime of impermeable and permeable tissue. Finally, Section 2.3 describes the two-compartment models evaluated in this simulation framework.

2.1 | Monte-Carlo simulations

2.1.1 | Simulations in permeable substrates

To simulate diffusion in permeable tissue,[30,38] we extended the MCDC Simulator.[29] In nonexchanging media, the diffusion process inside different biological structures is assumed to contribute independently to the DW-MRI signal. Consequently, the intracellular and extracellular signals are usually generated individually and summed to produce the total signal. In permeable substrates, some particles cross the membrane, which requires implementing multiple-diffusivity features to generate intracellular and extracellular signals simultaneously (see Data S1 for derivations). To minimize the boundary effects, we used a large voxel size and periodic boundary conditions when a particle crossed the voxel boundary.[29] After simulating the particles' trajectories, we generated the DW-MRI signals with a Graphics Processing Unit implementation for a PGSE sequence.

2.1.2 | Lymph nodes imaging

The application that motivates this study is the discrimination of healthy from cancerous lymph nodes using noninvasive imaging. Several studies investigated the potential of dMRI to replace invasive procedures such as biopsy for lymph node metastases diagnosis, particularly the apparent diffusion coefficient (ADC) in breast,[39,40] neck,[41] and colorectal[42] cancer, or more advanced biophysical models for benign and malignant tumor discrimination in lymph nodes.[17]

Figure 1 shows a Hematoxylin & Eosin (HE) stained slide of a colorectal cancer lymph node metastasis scanned using a 3DHistech Pannoramic P1000 digital slide scanner (at 20×). This tissue was fixed in 4% formalin and embedded in paraffin, following standard diagnostic protocols. Healthy lymph nodes (Figure 1, left magnification) are homogeneous tissues composed of round lymphocytes
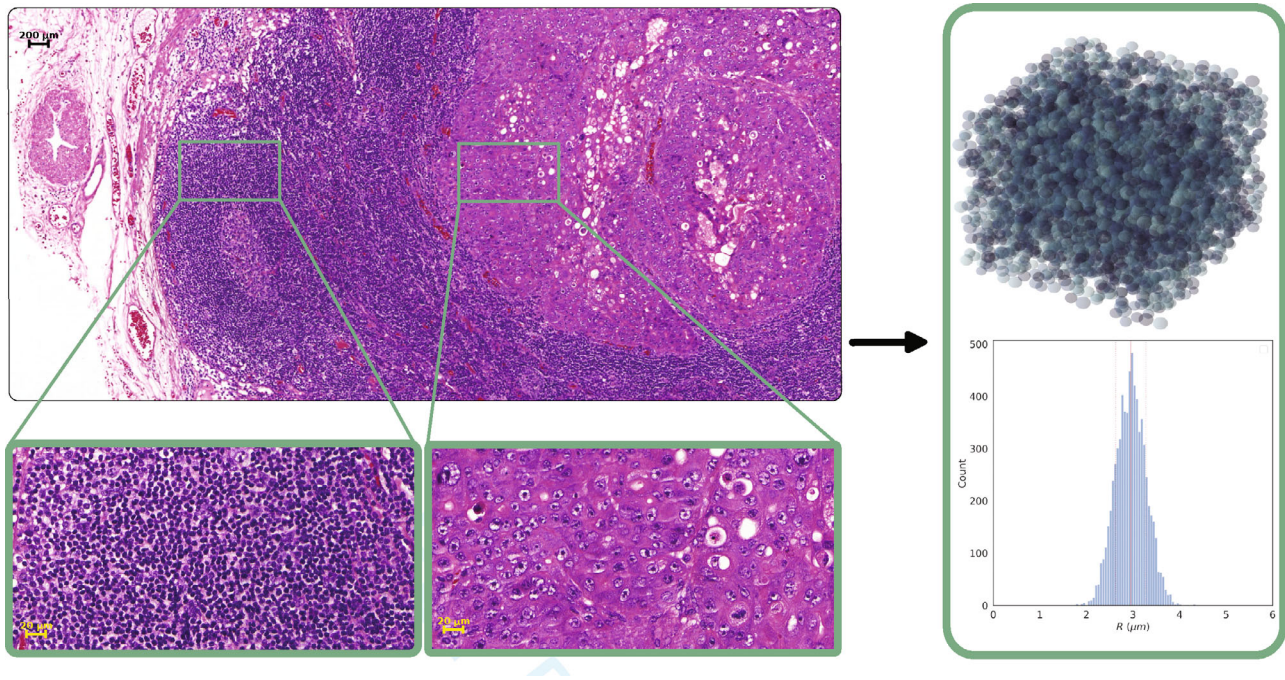
FIGURE 1 Lymph node histology and numerical substrate. Image of a Hematoxylin & Eosin stained slide of a colorectal cancer lymph node metastasis and a numerical substrate (Table 1) with a mean radius $R \simeq 3\mu m$. The histogram shows the radii distribution of the cells in the substrates. The solid red and dashed lines show the mean and the standard deviation of R, respectively.

that are known to be permeable.[43-45] We measured using QuPath[46] a cell area of $56 \pm 24\mu m^2$, corresponding to a radius from 3 to $5\mu m$ in perfectly spherical cells, similar to previously reported values.[17] In tumors (Figure 1, right magnification), the tissue is more heterogeneous with the presence of blood vessels and conjunctive tissue, with mean cell area of $225 \pm 102\mu m^2$, corresponding to cell radii from 6 to 10 μm.

The present work focuses on membrane permeability in spherical cells to capture the effect of exchange on microstructure estimation. Our substrates are isotropic, but a previous study[17] showed that the biophysical model that accounts for anisotropic diffusion had better results in lymph node discrimination. However, we decided to focus on the effect of exchange, and future work will combine exchange and anisotropic diffusion to better capture the complexity of lymph nodes' microstructure.

2.1.3 | Numerical substrates design

In addition to the rules of the particles' dynamic, MCDS required a numerical substrate into which the particles diffuse. As motivated in Section 2.1.2, we focus on numerical substrates made of packed spheres with finite membrane permeability.

We settled the substrates as isotropic voxels of side-length $100\mu m$, filled with randomly placed spheres.

These spheres had their radii normally distributed around a mean radius R_s equal to $\{2; 3; 4; 5; 8\}\mu m$ with a standard deviation of 1% of the radius. For all substrates, the intracellular volume fraction (ICVF) reached 0.65, corresponding to the value reported in malignant lymph nodes.[17]

Because the spheres in each substrate had different sizes, the apparent mean cell radius was weighted by the cell size distribution within the voxel. In the case of small cells, the apparent mean radius tends to $R_{small} = \left(\frac{<R^7>}{<R^3>}\right)^{\frac{1}{4}}$ at long diffusion times while, in the narrow-pulse approximation, the apparent mean radius becomes $R_{NP} = \left(\frac{<R^5>}{<R^3>}\right)^{\frac{1}{2}}$.[10] Table 1 summarizes the structural properties of the numerical substrates used in the experiments, and Figure 1 shows illustrative examples of the substrate S_2.

In addition to the structural properties, particles' trajectories depend on the biological properties of the substrates, which are the intracellular $D_{i,0}$ and extracellular $D_{e,0}$ diffusion coefficients and the membrane permeability κ. We chose their ranges in the simulations based on previously reported values for tumors[47] (Table 1).

2.1.4 | Sensitivity and reliability analysis of MCDS in permeable substrates

The first experiment aimed to evaluate the reliability and repeatability of the simulated signals with the substrates'

TABLE 1   Parameters of the Monte-Carlo diffusion simulations.

Substrate parameters					
	S_1	S_2	S_3	S_4	S_5
Voxel side length (μm)	100				
ICVF	0.65				
R_s (μm)	2	3	4	5	8
R_{mean} (μm)	1.9	3.0	4.0	5.0	8.1
R_{small} (μm)	2.2	3.1	4.1	5.1	8.3
R_{NP} (μm)	2.1	3.1	4.0	5.1	8.2
Simulation parameters					
$D_{e,0}$ (μm^2/ms)	$D_{i,0}$ (μm^2/ms)	κ (μm/s)	ρ (part/μm^3)	$\delta t(\mu s)$	
1, 2	1, 2	0, 10, 25, 50	0.5	5	
PGSE sequence parameters					
Δ(ms)	δ(ms)	TE(ms)	b (ms/μm^2)	N	
12, 20, 30, 40	4.5	50	1, 2.5, 4, 5.5, 7	24	

Notes: The experiments are detailed in Section 2. The voxel side length and the intracellular volume fraction (ICVF) are the same for all substrates. R_s is the desired mean cell radius of the sphere populations, R_{mean} is the effective mean cell radius, $R_{\text{small}} = \left(\frac{<R^7>}{<R^3>}\right)^{\frac{1}{4}}$ and $R_{NP} = \left(\frac{<R^5>}{<R^3>}\right)^{\frac{1}{2}}$.

biological properties (i.e., the permeability κ, the intracellular $D_{i,0}$ and the extracellular $D_{e,0}$ diffusion coefficients) described in the Section 2.1.3. We performed this sensitivity analysis with the substrate having a mean cell size of $2\mu m$ (Table 1, S_1), and we fixed the maximal particle density to $\rho = 2\mu m^{-3}$, that is, 2 millions of particles. The membrane permeability κ ranged from 0 to $50\mu m/s$, while we set the intracellular $D_{i,0}$ and extracellular $D_{e,0}$ diffusion coefficients to 1 or $2\mu m^2/ms$. For all combinations of these parameters, we calculated with bootstrapping the normalized mean square error (NMSEs) of the DW-MRI signals generated with the PGSE sequence (Table 1) in 24 uniformly distributed orientations on the unit sphere.

2.2 | From impermeable to permeable tissue

2.2.1 | Structural disorder in impermeable substrates

The apparent intracellular/extracellular diffusivities and kurtosis in impermeable tissue have distinct time-dependency. In the intracellular space, the water molecules are confined in the cells, and the apparent intracellular diffusivity ADC$_{\text{in}}(t)$ tends to 0. Conversely,

the water molecules of the extracellular space encounter obstacles but are free to diffuse. Therefore, the extracellular diffusivity ADC$_{\text{ex}}(t)$ converges to a nonzero long-time limit. Simultaneously, the kurtosis AKC$_{\text{ex}}(t)$ converges to zero, with a rate characterizing the mesoscopic disorder of the tissue.[48,49] In our substrates, the structural-disorder theory predicts that the impermeable ADC$_{\text{ex}}(t)$ and AKC$_{\text{ex}}(t)$ converge following $\propto t^{-1}$ (three-dimensional diffusion within short-range disorder represented by random spheres). Therefore, we fitted the equations ADC$_{\text{ex}}(t) = $ ADC$_\infty + A_D/t$ and AKC$_{\text{ex}}(t) = $ AKC$_\infty + A_K/t$ to the ADC$_{\text{ex}}(t)$ and AKC$_{\text{ex}}(t)$ calculated from the diffusion propagator (estimated from the spins trajectories in the media) for three substrates (Table 1 S_1, S_3, S_5) and two extracellular diffusion coefficients $D_{e,0} = \{1, 2\}\mu m^2/ms$. We chose those values according to simulation experiments of previous studies.[8,10,12,50,51]

Because tracking the particles' relative position in the substrate is possible with MCDS, we independently calculated the intracellular and extracellular diffusion coefficients and kurtosis. To this end, we assigned a particle to a compartment at initialization for the entire simulation. In permeable substrates, the particles cross the cell membranes and therefore, the intracellular and extracellular water interact, especially for high permeability values and long diffusion times. In this regime, interpreting the model parameters, like the diffusivities, is more

challenging since they are defined for water molecules residing inside the same compartment during the experimental time. Therefore, in the presence of exchange, we focused on the time-dependency of the ADC(t) and the AKC(t) (Section 2.2.2).

2.2.2 | Kärger assumptions validity in permeable substrates

The Kärger model of exchange is valid under two assumptions,[27] under which water diffuses in the barrier-limited regime. First, the diffusion inside each compartment is Gaussian, meaning the diffusion time is long enough for the particles to explore the compartment. This implies a time-independent diffusion coefficient. The second assumption links these characteristic times to membrane permeability by requiring slow exchange between the compartments, that is, the exchange time must be longer than the characteristic times of the compartments.

We determined the range of validity of the Kärger model using a time-dependency analysis of the ADC(t) and the AKC(t) of the same substrates as presented in Section 2.2.1 (Table 1, S_1, S_3, S_5) for different permeability values ($\kappa = \{0, 10, 25, 50\}\,\mu$m/s), spanning the parameter range considered in this work. From their time-dependencies, we quantified the effect of permeability on the estimated ADC(t) and AKC(t) for each experiment. Ultimately, we used these observations to discuss the validity of the model's assumptions (Section 4.2).

2.2.3 | Diffusion regime in the presence of exchange

In impermeable tissue, the tissue structure governs the diffusion dynamics. In the presence of exchange, the tissue structure and the exchange compete, producing different effects on the signal.[10] At a fixed diffusion encoding, that is, b-value, the evolution of the signal with the diffusion time is different whether the water exchange through the membrane or the restriction due to structure dominates. If the diffusion is barrier-limited, the Kärger model predicts a decreasing signal with the diffusion time.[27,33] Conversely, the signal increases if the restriction dictates the diffusion dynamics.[8,52]

To determine which effect dictates diffusion in our experiments, we generated DW-MRI signals with the PGSE sequence of Table 1 for the same parameters of the previous experiment (Section 2.2.2).

$$D_i(\Delta, \delta, R_s) = \frac{2}{\delta^2 D_{i,s}\left(\Delta - \frac{\delta}{3}\right)}\left[\sum_{m=1}^{\infty}\frac{\alpha_m^{-4}}{\alpha_m^2 R_s^2 - 2}\right.$$

$$\left.\left[2\delta - \frac{\begin{array}{c}2 + e^{-\alpha_m^2 D_{i,s}(\Delta-\delta)} - 2e^{-\alpha_m^2 D_{i,s}\delta}\\ - 2e^{-\alpha_m^2 D_{i,s}\Delta} + e^{-\alpha_m^2 D_{i,s}(\Delta+\delta)}\end{array}}{\alpha_m^2 D_{i,s}}\right]\right]. \quad (1)$$

2.3 | Compartmentalized models of microstructure

From Section 2.2, we identified the different diffusion regimes in our set of parameters. In this section, we describe two models of tumor microstructure: one designed for impermeable cellular tissue (Section 2.3.1) and one for permeable tissue (Section 2.3.2).

2.3.1 | Ball & Sphere diffusion: an impermeable model of tumors

Under the assumption of impermeable membranes, the extracellular and intracellular compartments were modeled independently. Diffusion inside the compartments was assumed to follow analytical equations that depended on their geometry.[37] We modeled the intracellular compartment as an impermeable sphere of radius R_s and intrinsic diffusivity $D_{i,s}$[52] having an apparent intracellular diffusion coefficient given by Equation 1, where α_m is the mth root of $(\alpha R_s) J_{\frac{3}{2}}(s\alpha R_s) = J_{\frac{5}{2}}(\alpha R_s)$ with $J_n(x)$ the Bessel function of the first kind, and extracellular diffusion with Gaussian isotropic diffusion of diffusivity D_e. Their respective volume fractions weighted the contribution of each compartment to the signal: $S_{\text{BALL\&SPHERE}} = (1 - f_i)e^{-bD_e} + f_ie^{-bD_i}$. This model had four parameters: the diffusion coefficients $D_{i,s}$, D_e, the cell size R_s and the intracellular volume fraction f_i.

2.3.2 | CEXI: a permeable model for spherical tumors

The model described in Section 2.3.1 is valid in impermeable substrates only. Conversely, our CEXI model is a two-compartment model that includes exchange based on the Kärger model[27] between an intracellular compartment that models spherical cells and an extracellular space. Similarly to the impermeable model, we modeled

the cells with a spherical compartment of radius R_s and intra-diffusivity $D_{i,s}$.

We assumed Gaussian and isotropic diffusion in the extracellular space with a diffusivity D_e. The water exchange rates from the intracellular to extracellular compartments k_i and from extracellular to intracellular k_e satisfied the spin conservation relation $k_i f_i = k_e(1 - f_i)$, where f_i is the intracellular volume fraction. In spherical cells, the exchange rate k_i and the membrane permeability κ are linked by the relation $k_i = (1 - f_i)(3\kappa/R_s)$.[33] Within this framework, the magnetization of the extracellular M_e and the intracellular M_i compartments follow the differential equations[28]

$$\begin{cases} \frac{dM_e}{dt} = -(q^2 D_e + k_e)M_e + k_i M_i, \\ \frac{dM_i}{dt} = k_e M_e - (q^2 D_{i,C}(t) + k_i)M_i, \end{cases} \quad (2)$$

with the initial conditions $M_e|_{t=0} = (1 - f_i)$ and $M_i|_{t=0} = f_i$, q^2 was the wavenumber of the PGSE sequence and $D_{i,C}(t)$ the time-dependent intracellular diffusivity. Ultimately, the signal was the weighted sum of these magnetizations $S_{CEXI} = (1 - f_i)M_e + f_i M_i$. With this formulation, CEXI had five parameters: the intracellular $D_{i,s}$ and extracellular D_e diffusion coefficients, the membrane permeability κ, the intracellular signal fraction f_i and the cell radius R_s.

Under Kärger assumptions, Equations (2) have an analytical solution.[9,12] However, the time-dependency of the intracellular diffusivity in large cells might invalidate this model. To guarantee the intracellular ADC_{in} follows Equation (1) at the diffusion times, we integrated Equations (2) for each diffusion time separately with a constant $D_{i,C}(\Delta) = D_i(\Delta)$. This approach allowed us to consider the time dependency of intracellular diffusivity empirically.

We acknowledge that the Kärger formulation is technically invalid in the case of time-dependent diffusion in one compartment, and our approach constituted an approximation similarly to previous studies.[9,12,33] This approximation was supported by the previous experiments (Section 3.2, Figure 4), where we showed that the $ADC_{ex}(t)$ in impermeable tissue converged quickly to its long-time limit to a value nearly independent of the cell size, conversely to the intracellular diffusivity, which converged more slowly to its long-time limit.

2.3.3 | Performance in permeable tissue

In this last experiment, we compared the performance of the impermeable Ball & Sphere model to the CEXI model. Because the numerical substrates of this work were made of spheres only, we did not include three-compartment models such as VERDICT[16] nor gray matter models that account for neurites.[8-10]

From the simulations described in Section 2.1, we selected the subset having an extracellular diffusivity of $2 \mu m^2/ms$. We generated the DW-MRI signals with the PGSE sequence described in Table 1. From the noise-free signals, we generated using the DIPY software library[53] 30 corrupted signals with Rician noise with a signal-to-noise (SNR) ratio of 30 and 80.

We fitted the models for all Δ simultaneously and accounted for the noise[54] with the constrained least squares implementation of the python optimization library LEVMAR.[55] We constrained the signal fractions to sum up to 1. We imposed boundaries on the value of the parameters to avoid unrealistic estimations: $\overline{R} \in [0.1, 20] \, \mu m$, $\overline{ICVF} \in [0.1, 0.9]$, $(\overline{D}_i, \overline{D}_e) \in [0.01, 3] \, \mu m^2/ms$, and $\kappa \in [0, \infty[\, \mu m/s$. We performed 10 optimizations with random initialization and selected the estimation that minimized the cost function.

We compared the models based on their estimates of the mean cell radius $\overline{R}$, intracellular volume fraction $\overline{ICVF}$ and extracellular $\overline{D}_e$ and intracellular $\overline{D}_i$ diffusion coefficients. We calculated the ground truth values of the intracellular volume fraction ICVF and the volume-weighted mean cell radius R from the substrates (Table 1). In Section 2.2, we showed that the apparent extracellular diffusion coefficient $ADC_{ex}(\Delta)$ deviated significantly from $D_{e,0}$ due to the obstacles encountered by the particles. Therefore, we considered as ground truth the D_e calculated from the propagator of the extracellular compartment at the longest diffusion time in the impermeable substrates (i.e., $D_e = ADC_{ex}(t = \Delta_{max}, \kappa = 0)$).

3 | RESULTS

3.1 | Influence of the substrate properties and the simulation parameters on the Monte-Carlo simulated DW-MRI signals

Figure 2 shows the evolution of the bootstrapped NMSE on the DW-MRI signals. For the given diffusion coefficients (Figure 2A), the NMSE increased with b and, at large b ($b > 4ms/\mu m^2$), the error became also dependent on Δ and κ. At fixed ($b = 2.5ms/\mu m^2$, $\Delta = 40$ ms) (Figure 2B), the diffusion coefficients had a distinct effect on the error. Indeed, the NMSE was dependent on $D_{e,0}$ (colors) while it seemed independent on $D_{i,0}$ (symbols). Figure 2C shows the decreasing rate of the NMSE with the particle density used in the simulations. Even with a particle density of $0.5 \mu m^{-3}$, the maximal error reached with the largest b, the longest Δ and the most permeable membrane remained under 1% with the chosen simulation parameters.
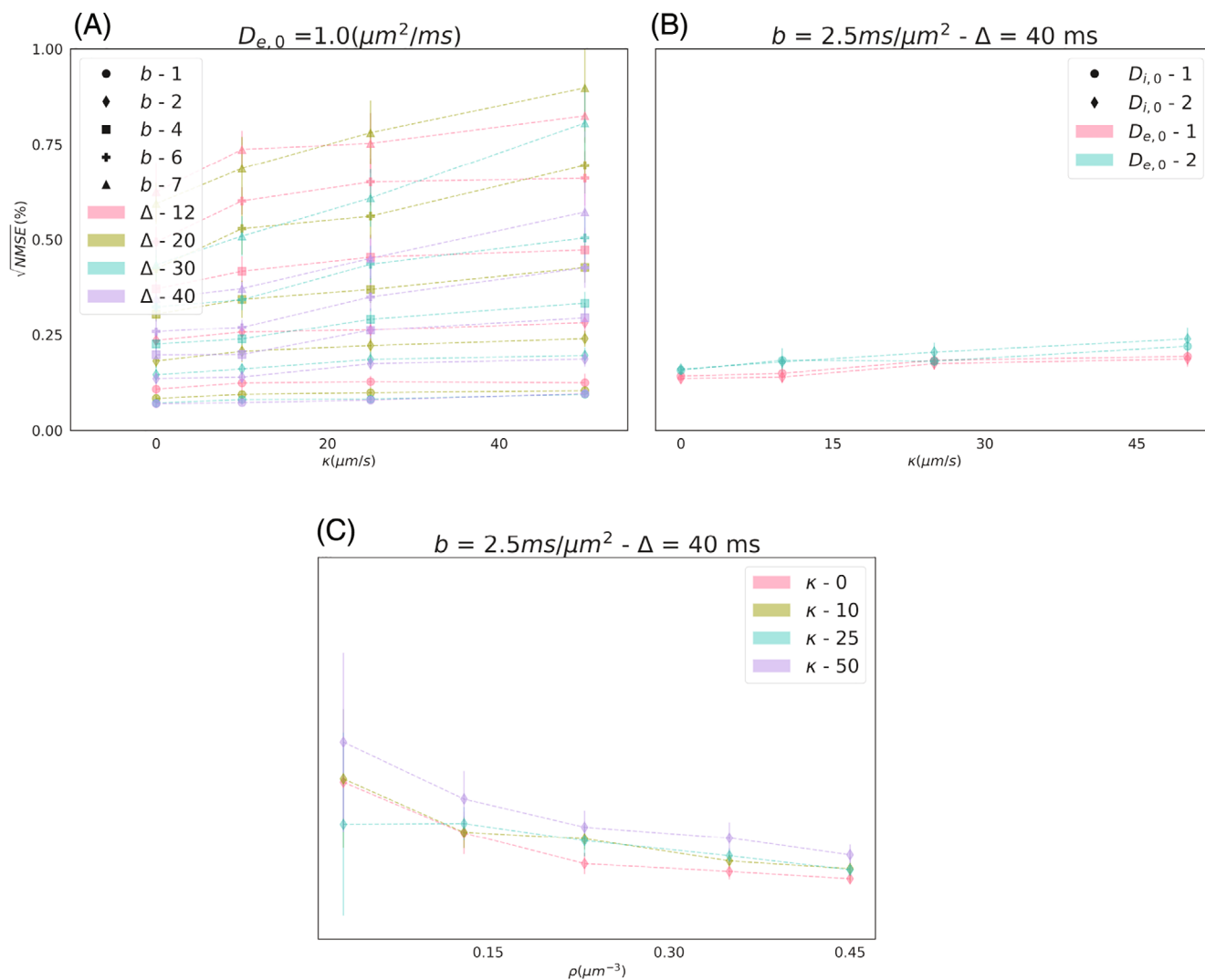
FIGURE 2 Normalized mean squared error on the signal. Normalised mean squared error (NMSE) on the signal with the permeability κ from bootstrapping for all pairs of b and diffusion time Δ (A), for all diffusion coefficients Δ (B) and different particle density (C). (A) The NMSE is shown for $D_{e,0} = 1\mu m^2/ms$ and $D_{i,0} = 2\mu m^2/ms$. The error increased with κ for all b - Δ pairs, and its range for different Δ broadened as b increased. (B) The NMSE is shown for the pair ($b = 2.5 ms\mu/m^2$, $\Delta = 40$ ms), for different $D_{e,0}$ (color) and $D_{i,0}$ (symbol). The error increased with $D_{e,0}$ but seemed independent on $D_{i,0}$. (C) The NMSE is plotted against the particle density used in the simulations for different permeability levels (color). Simulations with a faster permeability had a larger NMSE for all particle densities. The $\sqrt{\text{NMSE}}$ with the chosen simulation parameters never exceeded 1%.

3.2 | Mesoscopic disorder: time-dependency of ADC$_{ex}(t)$ and the AKC$_{ex}(t)$ in impermeable tissue

Figure 3 shows the time-dependency of the extra-cellular diffusion coefficient ADC$_{ex}(t)$ and kurtosis AKC$_{ex}(t)$ of the impermeable substrates S_1, S_3, and S_5, and the fitted parameters are summarized in Table 2. The rate of convergence of the ADC$_{ex}(t)$ depended on the cell size (symbols). In contrast, the long-time limits (ADC$_\infty$ and AKC$_\infty$ in Table 2) depended on the genuine extra-cellular diffusion coefficient $D_{e,0}$ (colors; Figure 3A and Table 2, D_∞). Conversely, the AKC$_{ex}(t)$ showed a convergence

rate that depended more on $D_{e,0}$ than the cell size (Figure 3D).

Figure 3B–D shows the ADC$_{ex}(t)$ and AKC$_{ex}(t)$ against t^{-1}, respectively, and the MSE is reported in Table 2.

3.3 | Kärger model: time-dependency of ADC(t) and the AKC(t) in permeable tissue

Figure 4 shows the evolution of extracellular ADC$_{ex}(t)$ and intracellular ADC$_{in}(t)$ diffusion coefficients of the impermeable substrates S_1, S_3, and S_5 along each other (A)
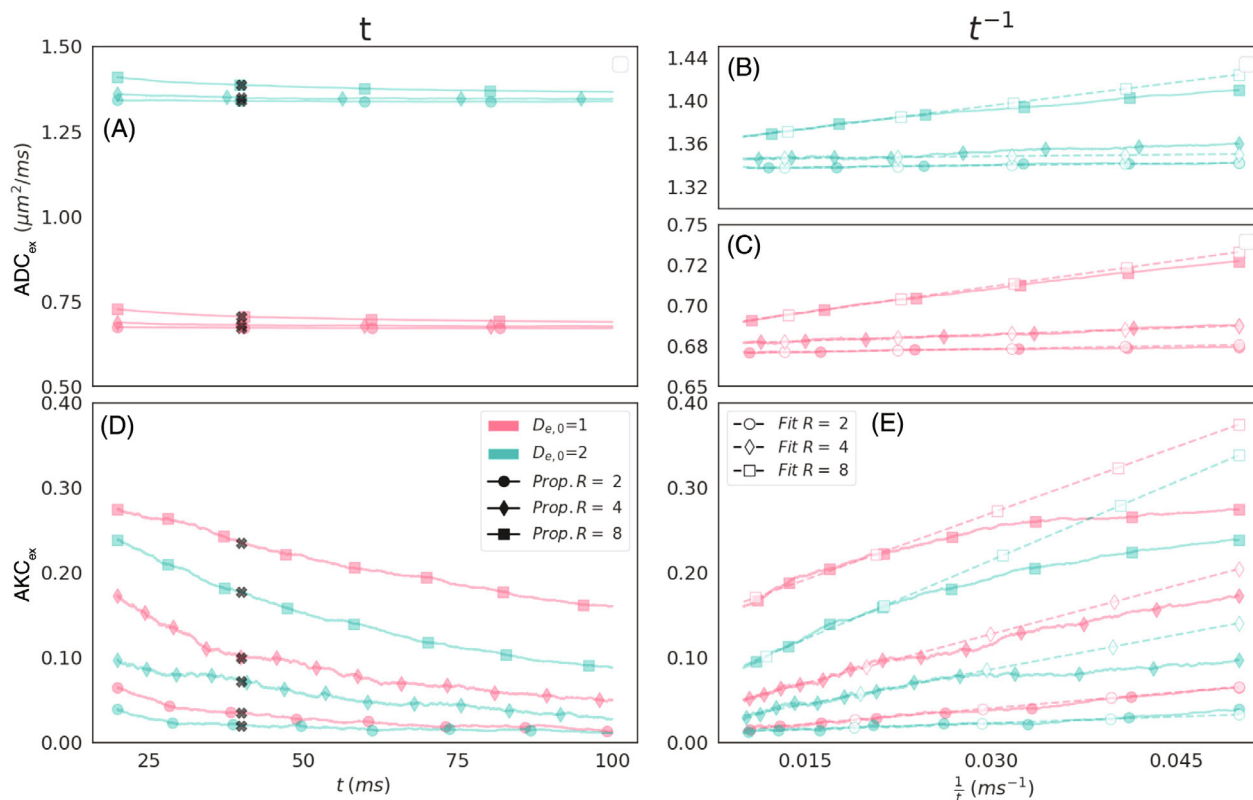
FIGURE 3 Extracellular $ADC_{ex}(t)$ and $AKC_{ex}(t)$ time-dependency in impermeable substrates. Time-dependency of the $ADC_{ex}(t)$ (A, B, C) and the $AKC_{ex}(t)$ (D, E) of the extracellular compartment of the substrate S_1 (circle), S_3 (diamond) and S_5 (square) (Table 1) without exchange calculated from the propagator, for different extracellular diffusion coefficient (color). (A) The ADC_{ex} was dependent on the extracellular diffusion coefficient but independent of the cell size. (D) Conversely, the time-dependency of the AKC_{ex} strongly depended on the extracellular diffusion coefficient and the cell size. (B, C) and E show the $ADC_{ex}(t)$ and $AKC_{ex}(t)$ against t^{-1} as predicted by the structural-disorder theory,[48,49] respectively. The white symbols show the fit of the corresponding function to the data. Because t^{-1} is decaying function of t, we fitted the equation in the decaying phase of the $ADC_{ex}(t)$ and $AKC_{ex}(t)$. The black crosses in A and D show the first point of the fitting.

TABLE 2 Results of the mesoscopic disorder fit.

Simulations		$ADC_{ex} = ADC_{\infty} + A_D/t$			$AKC_{ex} = AKC_{\infty} + A_K/t$		
R	$D_{e,0}$	A_D	ADC_{∞}	MSE_D	A_K	AKC_{∞}	MSE_K
2	1	0.00012	0.67	0.0002	1.25	0.003	0.0012
2	2	0.00012	1.33	0.0004	0.49	0.008	0.0001
4	1	0.00027	0.67	0.0005	3.84	0.013	0.0002
4	2	0.00011	1.34	0.0007	0.72	0.005	0.0020
8	1	0.00107	0.68	0.0003	5.21	0.113	0.0040
8	2	0.00144	1.35	0.0004	6.17	0.029	0.0027

Notes: Parameters of the curves shown in Figure 3. The cell size R is in μm, the extracellular diffusion coefficient $D_{e,0}$ and the parameters ADC_{∞}, MSE_D are in $\mu m^2/ms$, the parameter A_D is in μm^2 and the parameter A_K is in ms.

and their derivatives (B). As pointed out in Section 3.2, the $ADC_{ex}(t)$'s converged quickly to the same long-time limit. Conversely, the convergence rate of the intracellular $ADC_{in}(t)$'s depended on the cell size of the substrates.

The difference in decaying rate was confirmed by a large derivative of the intracellular diffusion coefficient for a longer diffusion time, in comparison to the extracellular $ADC_{ex}(t)$ (Figure 4B).
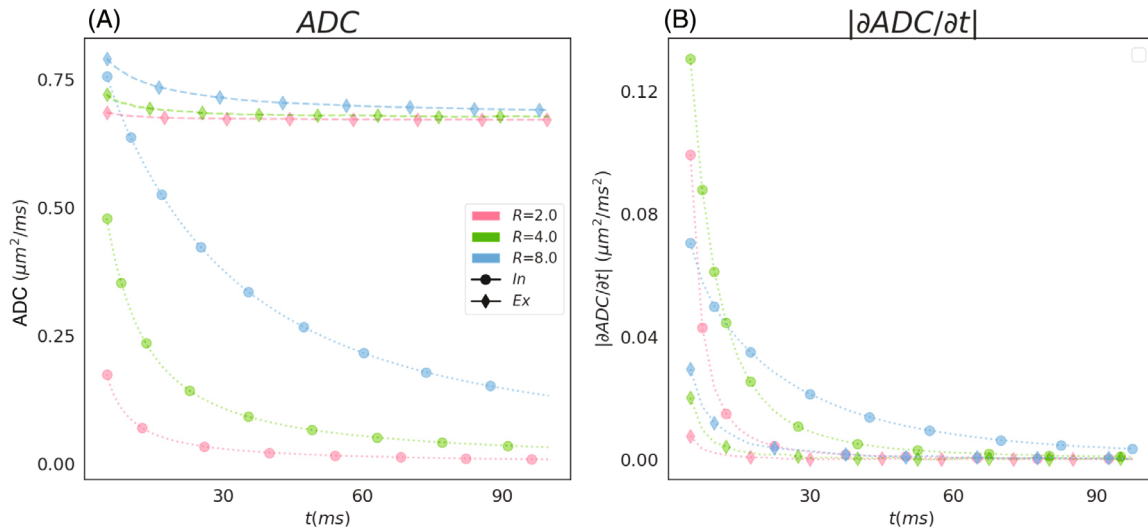
FIGURE 4 Extracellular $ADC_{ex}(t)$ and intracellular $ADC_{in}(t)$ time-dependency in impermeable substrates. (A) Time-dependency and (B) derivatives of the extracellular $ADC_{ex}(t)$ (diamond) and intracellular $ADC_{in}(t)$ (circle) of the substrate S_1 (red), S_3 (green) and S_5 (blue) (Table 1) without exchange calculated from the propagator. The intracellular $D_{i,0}$ and extracellular $D_{e,0}$ diffusion coefficient were equal to $1\mu m^2/ms$. (A) The $ADC_{ex}(t)$ converged faster than the $ADC_{in}(t)$ to its long-time limit. (B) Consequently, the rate of change $\partial ADC_{ex}/\partial t$ approached zero at short diffusion time, while the $\partial ADC_{in}/\partial t$ might not be negligible in our range of diffusion time.
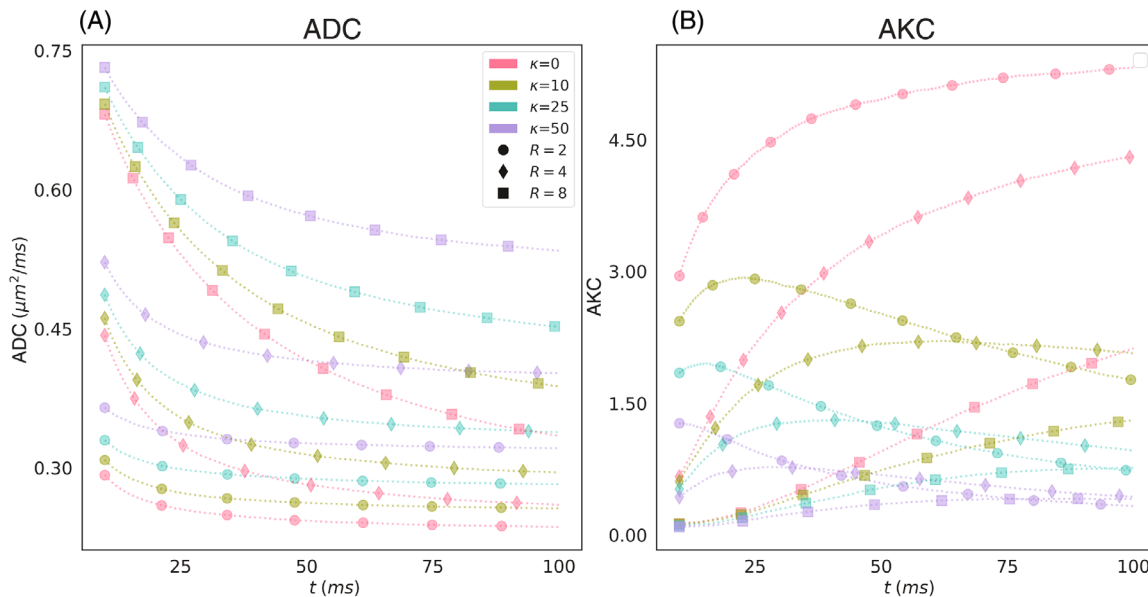

FIGURE 5 $ADC(t)$ and $ADK(t)$ time-dependency in permeable substrates. Time-dependency of the $ADC(t)$ (A) and $AKC(t)$ (B) in the three substrates S_1 (circle), S_3 (diamond) and S_5 (square) (Table 1) for an increasing permeability (color). The intracellular $D_{i,0}$ and extracellular $D_{e,0}$ diffusion coefficient were equal to $1\mu m^2/ms$. (A) As the permeability increased, the $ADC(t)$ converged faster to its long-time limit. (B) Simultaneously, the $AKC(t)$ reached its maximum value and, therefore, its decaying regime for a shorter diffusion time, except for the impermeable substrates and the permeable cells with the biggest radii where $AKC(t)$ always grew.

Figure 5 shows the results of the time-dependency analysis of the $ADC(t)$ and the $AKC(t)$ in impermeable and permeable substrates. In larger cells (symbols), the $ADC(t)$ converged to its long-time limit slowly (Figure 5A). This long-time limit of the $ADC(t)$ increased for an increasing permeability (colors).

In impermeable substrates, the $AKC(t)$ increased over the range of simulated time (Figure 5B). As soon as the membranes were permeable, the $AKC(t)$ exhibited a time dependency that could be split into two phases. The $AKC(t)$ increased to a peak value before decreasing to its long-time limit. This peak's location and

intensity depended on the cell size and the membrane's permeability.

3.4 | Diffusion regime: Barrier-limited or structure-limited?

Figure 6 shows the evolution of the signal with the diffusion time at a fixed b value. In the case of impermeable membranes (red), the signal increased with the diffusion time for all substrates and b values (symbols), as expected from restriction. Each substrate had a different diffusion regime as soon as the membranes were permeable. In the smallest spheres S_1 (Figure 6A), the signals of all b decreased with the diffusion time for all non-zero permeability values κ (colors), an exchange-dominated regime. In contrast, the signals of the largest spheres S_5 (Figure 6C) increased for all b and κ, a restriction-dominated regime. Finally, the signal of the substrate S_3 exhibited an intermediate regime (Figure 6B). At moderate permeability $\kappa < 25\mu$m/s, the signal increased with the diffusion time, while at the largest permeability, it increased at a short diffusion time before decreasing (Figure 6 blue, purple lines).

3.5 | Microstructure model estimates in permeable tissue

Figure 7 shows the substrate cell sizes R (A, E), intracellular volume fractions ICVF (B, F), extracellular D_e (C, G)

and intracellular D_i (D, H) diffusion coefficients estimated by the impermeable Ball & Sphere and CEXI models, and the CEXI estimate of the permeability (I). The markers and the bars are the means and variances of the estimates, respectively.

On the one hand, the impermeable Ball & Sphere model (Figure 7A-D) estimated the cell size, intracellular volume fraction and extracellular diffusion coefficient of all impermeable substrates accurately, except for the largest spheres (purple). At larger permeability, the impermeable Ball & Sphere model overestimated the cell size and underestimated the intracellular volume fraction more. Also, the estimated extracellular diffusivity decreased and stabilized at a smaller value. Finally, the impermeable Ball & Sphere model could not consistently estimate the intracellular diffusivity.

On the other hand, the CEXI model (Figure 7D–H) estimates of the cell size were consistent for all permeability values. CEXI slightly underestimated the small cell sizes (Figure 7, red, yellow, green) and overestimated the largest cell size (purple). Similarly, CEXI provided stable estimates of the intracellular volume fraction and extracellular diffusion coefficient in the small cell sizes from low to moderate permeability levels ($\kappa \leq 25\mu$m/s). CEXI tended to overestimate the true extracellular diffusion coefficient at increasing permeability, and the results were not accurate for permeability $\kappa \geq 25\mu$m/s. Finally, CEXI provided stable estimates of the intracellular diffusivity D_i in the substrates with a cell size $R > 3\mu$m.
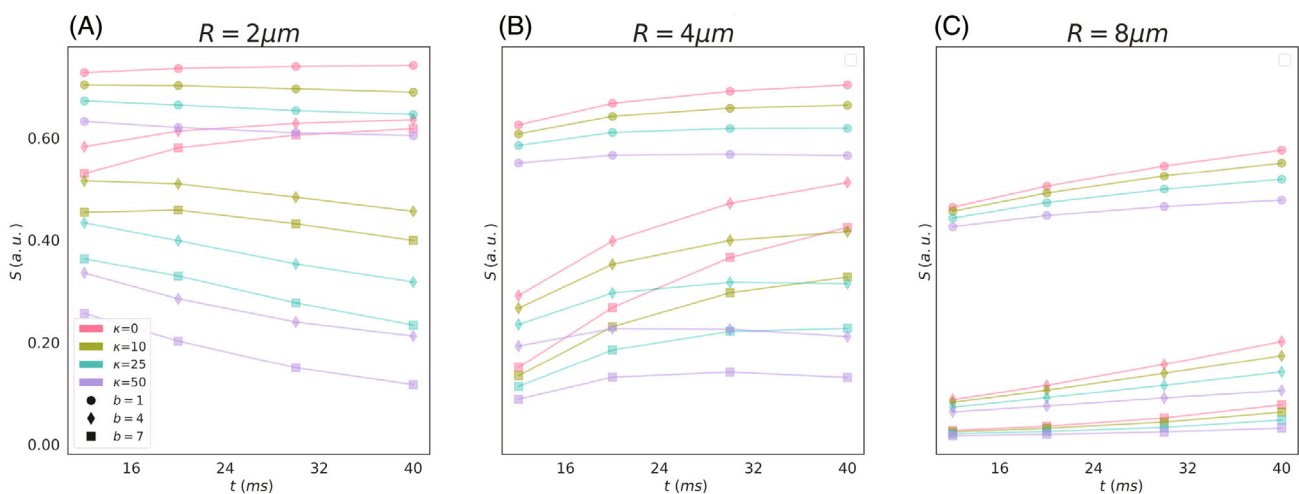

FIGURE 6 Evolution of the DW-MRI signal with the diffusion time at fixed b-value in permeable substrates. The plots show the evolution of the DW-MRI signal with the diffusion time at fixed b-value (symbols) for different permeability (color) in the substrates S_1 (A), S_3 (B) and S_5(C) (Table 1). (A) In substrate S_1, the signal decayed with the diffusion time for all b if the membranes were permeable. (C) Conversely, the signal increased for all b and permeability in the substrate S_5. (B) In the substrate S_3 having an intermediate cell size, the signal increased at slow permeability ($\kappa \leq 10\mu$m/s) but reached a plateau and started decreasing at faster permeability.
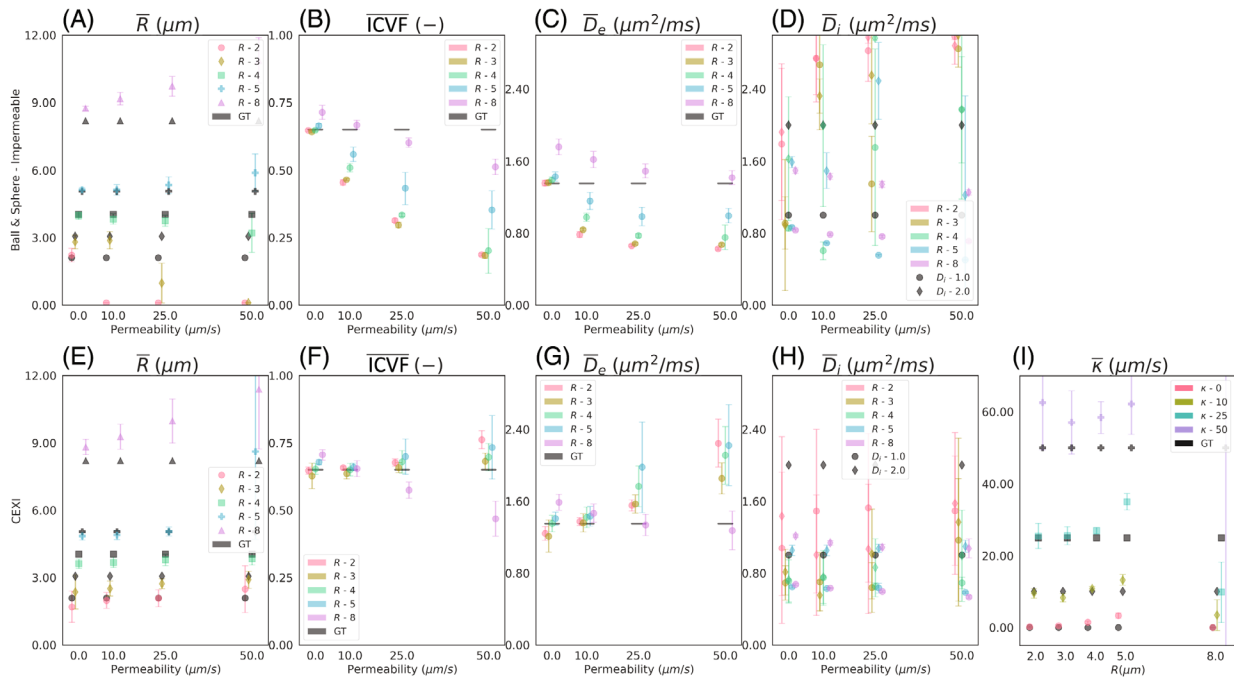
FIGURE 7 Model estimates. The plots show the estimates of the impermeable Ball & Sphere (A–D) and CEXI (E-I) models from 30 DW-MRI signals with an signal-to-noise ratio of 80. The estimates of the cell size (A, E), the intracellular volume fraction (B, F), the extracellular (C, G) and intracellular (D, H) diffusion coefficients are plotted against the permeability. The CEXI permeability estimate is plotted against the cell size (I). The color encodes the cell size (A-H) or the permeability (I), and the black lines show the ground truths of the substrate parameters. The symbols and the bars show the estimates' mean and variance, respectively.

In addition to these four parameters, CEXI estimated the exchange time τ_{ex} and, therefore, the permeability κ between the intracellular and extracellular compartments (Figure 7I). For all ground truth permeability values (color), the mean and the variance of the estimated permeability $\overline{\kappa}$ increased with the cell size and the true permeability. At moderate permeability $\kappa \leq 25 \mu \text{ms}$ and in the small cell size $R < 4 \mu \text{m}$, CEXI estimated the permeability accurately. For all parameters, a lower SNR led to a larger variance but comparable results (See Figures 7 and Figure S1 for the results with an SNR of 80 and 30, respectively).

4 | DISCUSSION

4.1 | Validation of the MCDS's in permeable tissue

This work investigated through realistic MCDS's the effect of membrane permeability κ on the estimation of microstructure model parameters in a model of permeable spheres. To perform simulations in permeable substrates, we extended the open-source MCDC diffusion simulator[29] following previous studies.[30,38]

4.1.1 | Repeatability of the signal generation

The permeability κ was identified as the first important substrate parameter that determined the choice of simulation parameters, to guarantee the repeatability of the simulation and a small NMSE, especially at a high b-value. The increase in the NMSE with κ was faster at high b, and the NMSE range for different diffusion times Δ broadened as b increased. This suggests that the particle density required for the simulations was more dependent on b and κ than Δ. In parallel, the extracellular diffusion coefficient $D_{e,0}$ was shown to play a major role in signal generation, which confirmed that both intracellular and extracellular signals must be simulated simultaneously. Despite the increase in the NMSE with κ and b, the small error ($\sqrt{\text{NMSE}} < 1\%$) of the signals validated the choice of the simulation parameters (Table 1) of the experiments.

4.1.2 | Is the simulated signal consistent?

Simultaneously, a time-dependency analysis of the apparent diffusivity and kurtosis in impermeable substrates validated the correct implementation of the simulations by comparing to theoretically expected trends.

In the intracellular space, the $ADC_{in}(t)$ of the particles confined inside the cells converged to 0 at a rate dependent on the cell size. In the extracellular space, the diffusion coefficient $ADC_{ex}(t)$ converged quickly to its long-time limit both in small and large spheres. Interestingly, this long-time limit depended on the packing density of the substrate rather than the cell size. The convergence rate of the $ADC_{ex}(t)$ and the kurtosis $ADK_{ex}(t)$ were consistent with the power-law of t^{-1} predicted by structural disorder in a 3D environment of spheres (short-range 3D disorder)[48,49] in the long time limit.

4.1.3 │ Diffusion regime in tissues of different permeability and cell sizes

In permeable substrates, the physical interpretation of the $ADC_{in}(t)$ and the $ADC_{ex}(t)$ became ambiguous, and we focused our attention on the total $ADC(t)$ and $AKC(t)$. At larger permeability values, the mixing rate of the compartments increased, and the $ADC(t)$ converged faster. Similarly, the time dependency of the $AKC(t)$ depended on the permeability. As the permeability increased, the peaking time of the $AKC(t)$ shifted to shorter diffusion times, coherently with previous work.[25,56]

Permeability added another degree of freedom to the diffusion regime, which modulated the DW-MRI signal. Following recent work,[10] we showed that the effects of exchange and restriction competed in the signal dynamic. For the cell sizes investigated in this work, the extremes had a clear but distinct diffusion regime. The water exchange dominated the diffusion dynamic in small spheres, while the restriction dominated in substrates with large spheres. Interestingly, the intermediate cell size exhibited a shift of diffusion dynamic at higher permeability between exchange and structure. The permeability at which this shift occurred ($\kappa = 25\mu m/s$) corresponds to the minimal permeability value for which the $AKC(t)$ reached its peak in the range of diffusion time of the PGSE sequence, independently of the b-value. In other words, the diffusion time at which the diffusion regime shifted from restriction-dominated to exchange-dominated corresponded to the maximal value of the kurtosis $AKC(t)$. Therefore, it should be possible to determine the minimal diffusion time to enter the exchange-dominated diffusion regime from kurtosis measurements at multiple diffusion times. This provides a way to choose the parameters of the PGSE sequence in experiments, especially the minimal diffusion time, to become sensitive to the microstructure feature of most interest. However, we noted that, experimentally, the range of achievable diffusion times might also depend on hardware limitations.

4.2 │ Compartmentalized models in permeable substrates of tumors

The last experiment compared the impermeable Ball & Sphere model to our CEXI model, which included the water exchange. Previous studies demonstrated that estimating the substrate's properties with compartmentalized models is a challenging ill-posed problem. The low sensitivity of these models to the compartment diffusivities was highlighted in white matter[13,57] and, more recently in gray matter.[8-10] Additionally, the size of the axons in white matter[49] or the cells in gray matter[10,50,58] was shown to be overestimated. This experiment showed the impact of permeability on the estimated model parameters, including the mean cell radius $\overline{R}$, extracellular $\overline{D}_e$ and intracellular $\overline{D}_i$ diffusion coefficients and intracellular volume fraction $\overline{ICVF}$.

4.2.1 │ Cell size and intracellular volume fraction estimation

The impermeable Ball & Sphere model accurately estimated the substrates parameters in the impermeable substrates, except for D_i. It overestimated and underestimated the cell size R and the intracellular volume fraction ICVF as permeability increased, respectively.[10,50] This opposite evolution indicated how the models developed for impermeable tissues compensated for water exchange. Because the cell size limited the distance traveled by the particles in impermeable cells, the increase in diffusion distance due to permeability was compensated by either decreasing the proportion of the intracellular signal via a smaller $\overline{ICVF}$ or increasing the maximal distance via a larger $\overline{R}$. This deterioration of the estimates was more significant for smaller cells, which is coherent with the observation that diffusion enters the exchange-dominated regime at a shorter diffusion time.

On the other hand, this effect was attenuated with the CEXI model, thanks to the exchange time capturing most of the exchange effect. At moderate permeability ($\kappa < 25\mu m/s$), CEXI disentangled the effect of exchange and restriction from the DW-MRI signals, providing more stable estimates of $\overline{ICVF}$ and $\overline{R}$ with the cell size and the permeability than the impermeable Ball & Sphere model over this range of permeability. When diffusion was dominated by exchange, i.e. in the small cells $R < 5\mu m$, the mean cell size and the intracellular volume fraction were better estimated. When diffusion was not dominated by the exchange yet ($R > 5\mu m$), the $ADC(t)$ was strongly time-dependent, and the CEXI model assumptions were not valid. Consequently, the intracellular volume fraction estimates were less stable as a function of permeability.

4.2.2 | Sensitivity to the compartment diffusivity variations

The compartment diffusivities were arguably the most difficult parameters to estimate due to the degeneracy of the solution[6,57] and the low sensitivity of the models to the intracellular diffusion coefficient.[13] In white matter, the intracellular diffusion coefficient was often considered faster than the extracellular diffusion coefficient.[59-61] Still, recent studies in gray matter suggested contradictory conclusions on which compartment had the fastest diffusivity ($D_e > D_i$ in ex vivo[10] or $D_e < D_i$ in in vivo[9]). In our experiments, the impermeable model highlighted this degeneracy of the solution through unstable or estimates of the diffusivities.

Conversely, the CEXI model showed sensitivity to D_e and D_i changes with a limited impact on the estimates $\overline{R}$ and $\overline{ICVF}$, supporting that the contribution of each compartment to the total signal could be disentangled by including an exchange parameter in the model. At moderate permeability ($\kappa \leq 25\mu$m/s) and in the larger spheres ($R > 3\mu$m), CEXI was sensitive to the variations of the intracellular diffusion coefficient. In the small spheres ($R < 3\mu$m), however, the cells were too small for CEXI to be sensitive to D_i. Indeed, diffusion inside the intracellular compartment reached the Gaussian diffusion limit before the shortest diffusion time, irrespective of the true D_i.

4.2.3 | Permeability estimate

In the previous section, we identified exchange-dominated and restriction-dominated regimes. We determined that the transition between those regimes occurred for the substrates of cell size around 4–5 μm. In smaller cells, the exchange dominates; therefore, we should be sensitive to membrane permeability. The accurate estimation of the permeability with CEXI in this range of cell sizes confirmed this observation. At moderate permeability ($\kappa \leq 25\mu$m/s), CEXI estimated the permeability accurately with a small variance. The best estimates were obtained for substrates in the transition regime, that is, cells of size 4–5 μm. In larger cells, the estimates' variance was too large to be reliable.

4.3 | Recommendations

In Sections 4.1 and 4.2, we showed the importance of probing tissue in the correct diffusion time frame. In permeable tissue, diffusion translates from a restriction-dominated to an exchange-dominated regime at a long enough diffusion time. To find a good range of diffusion times for the

tissue under consideration, a preliminary time-dependency analysis of the apparent diffusion coefficient ADC(t) and kurtosis AKC(t) might be insightful. Indeed, we showed that diffusion moves from the restriction-dominated to the exchange-dominated regime at the peak value of the AKC(t). Our CEXI model provided more robust estimates in this exchange-dominated regime than the impermeable Ball & Sphere model in permeable substrates. In the largest cells or at high permeability values, estimation remained challenging even with CEXI. In the first case, diffusion was dominated by structure and not exchange. In the second case, the exchange was too fast. This finding suggested that future models should be developed by generalizing the assumptions behind the Kärger model to accurately estimate the microstructure parameters in highly permeable tissue. These observations show that the PGSE sequence is suitable for a specific exchange time. Alternative sequences, such as double-diffusion encoding[62,63] or stimulated echo sequence,[12] might be better adapted for tissue with a longer exchange time. On the other hand, oscillatory gradient spin echo sequence[11] showed promising results in tissue with shorter exchange time.

4.4 | Toward lymph nodes imaging

Based on previous conclusions and histology data, we could design a protocol for real DW-MRI data acquisitions on lymph nodes. The lymphocyte radius is around 3-5 μm, so the molecular diffusion in the lymphocytes should already be in the exchange regime at a diffusion time of about 30 ms We could determine the lymphocyte permeability by comparing acquisitions to the simulations. In the example of malignant lymph nodes shown in Figure 1, the cells are bigger with a radius around 6-10 μm. Hence, diffusion will be in the restriction-dominated regime for a diffusion time under 30 ms. We plan to acquire data with a longer diffusion time until we reach the exchange-dominated regime. We expect this threshold diffusion time to be correlated with cancerous tissue. Future work will combine membrane permeability and anisotropic diffusion to capture better the complexity of lymph node microstructure[17] and, consequently, determine if a model with more compartments is needed.[28]

5 | CONCLUSION

This work showed, using simulations in numerical substrates of packed spheres, that the water exchange between the intracellular and extracellular spaces cannot be neglected in permeable tissues when diffusion is

in the exchange-dominated regime. The time-dependency of the kurtosis and the signal could be used to identify the dominating diffusion regime and, ultimately, the most relevant biophysical model and the experimental parameters of the imaging protocol best suited to estimate its parameters. Additionally, the inherent bias in the estimates of the compartmentalized models for impermeable tissue was amplified in permeable tissue, even for very low permeability values. As an alternative, a two-compartment model of permeable tumors considering the water exchange between spherical cells and the extracellular space was evaluated, allowing us to simultaneously estimate the exchange time and cell size. Despite the improved performance compared to the impermeable model in the regime from low to moderate permeability levels, some limitations were found in highly permeable substrates, suggesting the need for a more general model of permeable tissue that accounts for the non-Gaussian diffusion in the compartments and the time-dependency of the diffusion coefficients.

AUTHOR CONTRIBUTIONS

Rémy Gardier: Methodology, Coding, Simulations, Analysis, Writing, Visualization, **Juan Luis Villarreal Haro**: Discussion about substrate generation and the choice of the parameters of the simulation, Writing - Review, **Erick J. Canales-Rodríguez**: Methodology, Writing-Review and Editing, **Ileana O. Jelescu**: Discussion about the compartmentalized model and mesoscopic disorder theory, Writing-Review and Editing, **Gabriel Girard**: Methodology, Experimental design, Writing-Review and Editing, **Jonathan Rafael-Patiño**: Methodology, Experimental design, Discussion about simulations, Active contribution to the analysis of the results, Supervision, Writing - Review and Editing, **Jean-Philippe Thiran**: Supervision, Funding, Writing-Review.

CONFLICT OF INTEREST STATEMENT
The authors declare that the research was conducted in the absence of any commercial or financial relationships that could be construed as a potential conflict of interest.

DATA AVAILABILITY STATEMENT
The data used for this manuscript were simulated with an extension of the open-source Monte-Carlo simulator (https://jonhrafe.github.io/MCDC_Simulator_public/) and can be shared upon request by emailing the corresponding author.

ORCID
Rémy Gardier https://orcid.org/0000-0001-6073-0812
Erick J. Canales-Rodríguez https://orcid.org/0000-0001-6421-2633
Ileana O. Jelescu https://orcid.org/0000-0002-3664-0195
Gabriel Girard https://orcid.org/0000-0002-5781-3104
Jonathan Rafael-Patiño https://orcid.org/0000-0002-8960-5465
Jean-Philippe Thiran https://orcid.org/0000-0003-2938-9657

REFERENCES
1. Alexander DC, Hubbard PL, Hall MG, et al. Orientationally invariant indices of axon diameter and density from diffusion MRI. *Neuroimage*. 2010;52:1374-1389.
2. Hui Z, Torben S, Wheeler-Kingshott Claudia A, Alexander DC. NODDI: practical in vivo neurite orientation dispersion and density imaging of the human brain. *Neuroimage*. 2012;61:1000-1016.
3. Jespersen SN, Kroenke CD, Leif Ø, Ackerman Joseph JH, Yablonskiy DA. Modeling dendrite density from magnetic resonance diffusion measurements. *Neuroimage*. 2007;34:1473-1486.
4. Maira T, Torben S, Alexander DC, Wheeler-Kingshott CA, Gandini ZH. Bingham-NODDI: mapping anisotropic orientation dispersion of neurites using diffusion MRI. *Neuroimage*. 2016;133:207-223.
5. Enrico K, Kelm ND, Carson RP, Does MD, Alexander DC. Multi-compartment microscopic diffusion imaging. *Neuroimage*. 2016;139:346-359.
6. Novikov DS, Jelle V, Jelescu IO, Els F. Rotationally-invariant mapping of scalar and orientational metrics of neuronal microstructure with diffusion MRI. *Neuroimage*. 2018;174:518-538.
7. Novikov DS, Els F, Jespersen SN, Kiselev VG. Quantifying brain microstructure with diffusion MRI: theory and parameter estimation. *NMR Biomed*. 2019;32:37-54.
8. Marco P, Andrada I, Michele G, et al. SANDI: a compartment-based model for non-invasive apparent soma and neurite imaging by diffusion MRI. *Neuroimage*. 2020;215:116835.
9. Jelescu IO, Alexandre S, Françoise G, Marco P, Novikov DS. Neurite exchange imaging (NEXI): a minimal model of

diffusion in gray matter with inter-compartment water exchange. *Neuroimage*. 2022;256:119277.

10. Olesen JL, Leif Ø, Noam S, Jespersen SN. Diffusion time dependence, power-law scaling, and exchange in gray matter. *Neuroimage*. 2022;251:2-4.

11. Olivier R, Veronica WK, Minh HD, Zaim WY, Novikov DS, Gene KS. Pulsed and oscillating gradient MRI for assessment of cell size and extracellular space (POMACE) in mouse gliomas. *NMR Biomed*. 2016;29:1350-1363.

12. Gogulan K, Wheeler RJ, Tear LR, Farrer NJ, Stephen F, Baldwin AJ. INDIANA: an in-cell diffusion method to characterize the size, abundance and permeability of cells. *J Magn Reson*. 2019;302:1-13.

13. Hua L, Xiaoyu J, Jingping X, Gore JC, Junzhong X. Impact of transcytolemmal water exchange on estimates of tissue microstructural properties derived from diffusion MRI. *Magn Reson Med*. 2017;77:2239-2249.

14. Xiaoyu J, Hua L, Jingping X, et al. In vivo imaging of cancer cell size and cellularity using temporal diffusion spectroscopy. *Magn Reson Med*. 2017;78:156-164.

15. Olivier R, Veronica WK, Minh HD, Zaim WY, Novikov DS, Gene KS. Surface-to-volume ratio mapping of tumor microstructure using oscillating gradient diffusion weighted imaging. *Magn Reson Med*. 2016;76:237-247.

16. Eletheria P, Simon W-S, Bernard S, et al. Noninvasive quantification of solid tumor microstructure using VERDICT MRI. *Cancer Res*. 2014;74:1902-1912.

17. Andrada I, Ines S, Antonio G, et al. Higher-order diffusion MRI characterization of mesorectal lymph nodes in rectal cancer. *Magn Reson Med*. 2020;84:348-364.

18. Sahalan M. Diffusion-Weighted Imaging of Lymph Node Tissue. Thesis. University of Sydney. 2018.

19. Mami I, Olivier R, Tomokazu T, et al. Characterization of glioma microcirculation and tissue features using intravoxel incoherent motion magnetic resonance imaging in a rat brain model. *Invest Radiol*. 2014;49:485-490.

20. Jelescu IO, Marco P, Francesca B, Schilling KG. Challenges for biophysical modeling of microstructure. *J Neurosci Methods*. 2020;344:108861.

21. Yang Donghan M, Huettner James E, Larry BG, Neil Jeffrey J, Garbow Joel R, Ackerman Joseph JH. Intracellular water pre-exchange lifetime in neurons and astrocytes. *Magn Reson Med*. 2018;79:1616-1627.

22. Zhao L, Kroenke CD, Song J, Piwnica-Worms D, Ackerman JJH, Neil JJ. Intracellular water-specific MR of microbead-adherent cells: the HeLa cell intracellular water exchange lifetime. *NMR Biomed*. 2008;21:159-164.

23. Olivier R. Time-dependent diffusion MRI in cancer: tissue modeling and applications. *Front Phys*. 2017;5:58.

24. Xiaoyu J, Devan SP, Jingping X, Gore JC, Junzhong X. Improving MR cell size imaging by inclusion of transcytolemmal water exchange. *NMR Biomed*. 2022;35:4-6.

25. Manisha A, Smith MD, Calabresi PA. Diffusion-time dependence of diffusional kurtosis in the mouse brain. *Magn Reson Med*. 2020;84:1564-1578.

26. Samo L, Markus N, Jimmy L, Freddy S, Daniel T. Apparent exchange rate mapping with diffusion MRI. *Magn Reson Med*. 2011;66:356-365.

27. Jörg K. NMR self-diffusion studies in heterogeneous systems. *Adv Colloid Interface Sci*. 1985;23:129-148.

28. Stanisz GJ, Aaron S, Wright GA, Mark HR. An analytical model of restricted diffusion in bovine optic nerve. *Magn Reson Med*. 1997;37:103-111.

29. Jonathan R-P, David R, Alonso R-M, Jorge C-RE, Gabriel G, Philippe TJ. Robust Monte-Carlo simulations in diffusion-MRI: effect of the substrate complexity and parameter choice on the reproducibility of results. *Front Neuroinform*. 2020;14:8.

30. Hsi LH, Els F, Novikov DS. Realistic microstructure simulator (RMS): Monte Carlo simulations of diffusion in three-dimensional cell segmentations of microscopy images. *J Neurosci Methods*. 2021;350:6.

31. Hall MG, Alexander DC. Convergence and parameter choice for Monte-Carlo simulations of diffusion MRI. *IEEE Trans Med Imaging*. 2009;28:1354-1364.

32. Lorenza B, Gloria M, Markus N. Monte Carlo simulations of water exchange through myelin wraps: implications for diffusion MRI. *IEEE Trans Med Imaging*. 2019;38:1438-1445.

33. Els F, Novikov DS, Jensen JH, Helpern JA. Monte Carlo study of a two-compartment exchange model of diffusion. *NMR Biomed*. 2010;23:711-724.

34. Ali A, Ilya B, Eija J, Jussi T, Alejandra S. Automated 3D axonal morphometry of white matter. *Sci Rep*. 2019;9:1-16.

35. Hsi LH, Antonios P, Lyoung KS, Novikov Dmitry S, Els F. A time-dependent diffusion MRI signature of axon caliber variations and beading. *Commun Biol*. 2020;3:1-13.

36. Mariam A, Martin KH, Jonathan R-P, et al. Axon morphology is modulated by the local environment and impacts the noninvasive investigation of its structure-function relationship. *Proc Natl Acad Sci U S A*. 2020;117:33649-33659.

37. Eleftheria P, Torben S, Bernard S, Hall Matt G, Lythgoe Mark F, Alexander DC. Compartment models of the diffusion MR signal in brain white matter: a taxonomy and comparison. *Neuroimage*. 2012;59:2241-2254.

38. Aaron S, Jianhui Z, Gore JC. Theoretical model for water diffusion in tissues. *Magn Reson Med*. 1995;33:697-712.

39. Fatma Z, Shehata SM, Warda MH, Abo Wardo MH, Alekrashy MA. Diagnostic value of MRI for predicting axillary lymph nodes metastasis in newly diagnosed breast cancer patients: diffusion-weighted MRI. *Egypt J Radiol and Nucl Med*. 2016;47:659-667.

40. Zhao M, Wu Q, Guo L, Zhou L, Radiology KF. *European Journal, 2020. Magnetic Resonance Imaging Features for Predicting Axillary Lymph Node Metastasis in Patients with Breast Cancer*. Elsevier; 2020.

41. Suh CH, Choi YJ, Baek JH, Lee JH. The diagnostic value of diffusion-weighted imaging in differentiating metastatic lymph nodes of head and neck squamous cell carcinoma: a systematic review and meta-analysis. *Am J Neuroradiol*. 2018;39:1889-1895.

42. Yasui O, Sato M. Experimental a Kamada the Tohoku, 2009. Diffusion-weighted imaging in the detection of lymph node metastasis in colorectal cancer. *Jstagejstgojp*. 2009;218:177-183.

43. Cheung RK, Grinstein S, Gelfand EW. Volume regulation by human lymphocytes. Identification of differences between the two major lymphocyte subpopulations. *J Clin Investig*. 1982;70:632-638.

44. Grinstein S, Clarke CA, Rothstein A, Gelfand EW. Volume-induced anion conductance in human B lymphocytes is cation independent. *Am J Physiol Cell Physiol*. 1983;245:C160-C163.

45. Sebastian W, Dieter K. Activation-driven death of human T cell clones: time course kinetics of the induction of cell shrinkage, DNA fragmentation, and cell death. *Cell Immunol.* 1993;148:234-241.

46. Bankhead P, Loughrey MB, Fernandez JA, et al. QuPath: open source software for digital pathology image analysis. *Sci Rep.* 2017;7:1-7.

47. Mukherjee A, Wu D, Hunter CD, Shapiro MG. Non-invasive imaging using reporter genes altering cellular water permeability. *Nat Commun.* 2016;7:13891.

48. Novikov DS, Jensen JH, Helpern JA, Els F. Revealing mesoscopic structural universality with diffusion. *Proc Natl Acad Sci U S A.* 2014;111:5088-5093.

49. Burcaw LM, Els F, Novikov DS. Mesoscopic structure of neuronal tracts from time-dependent diffusion. *Neuroimage.* 2015;114:18-37.

50. Maryam A, Markus N, Marco P, Jones DK. SPHERIOUSLY? The challenges of estimating sphere radius non-invasively in the human brain from diffusion MRI. *Neuroimage.* 2021;237:118183.

51. Elisenda B-C, Edward J, Alessandro D, et al. VERDICT-AMICO: ultrafast fitting algorithm for non-invasive prostate microstructure characterization. *NMR Biomed.* 2019;32:e4019.

52. Neuman CH. Spin echo of spins diffusing in a bounded medium. *J Chem Phys.* 1974;60:4508-4511.

53. Eleftherios G, Matthew B, Bagrat A, et al. Dipy, a library for the analysis of diffusion MRI data. *Front Neuroinform.* 2014;8:8.

54. Alexander DC. A general framework for experiment design in diffusion MRI and its application in measuring direct tissue-microstructure features. *Magn Reson Med.* 2008;60:439-448.

55. Lourakis MIA. Levmar: Levenberg-Marquardt nonlinear least squares algorithms in {C}/{C}++. 2004.

56. Jin Z, Gregory L, Linda M, Els F, Novikov DS, Gene KS. Measurement of cellular-interstitial water exchange time in tumors based on diffusion-time-dependent diffusional kurtosis imaging. *NMR Biomed.* 2021;34:e4496.

57. Jelescu IO, Jelle V, Els F, Novikov DS. Degeneracy in model parameter estimation for multi-compartmental diffusion in neuronal tissue. *NMR Biomed.* 2016;29:33-47.

58. Marco P, Alexander Daniel C, Hui Z. Large-scale analysis of brain cell morphometry informs microstructure modelling of gray matter. *Proc Int Soc Magn Reson Med.* 2021;Abstract 0642.

59. Nicolas K, Silva AR, Jelescu IO. Intra- and extra-axonal axial diffusivities in the white matter: which one is faster? *Neuroimage.* 2018;181:314-322.

60. Bibek D, Marco R, Elias K, Kiselev VG. Intra-axonal diffusivity in brain white matter. *Neuroimage.* 2019;189:543-550.

61. Olesen JL, Leif Ø, Noam S, Jespersen SN. Beyond the diffusion standard model in fixed rat spinal cord with combined linear and planar encoding. *Neuroimage.* 2021;231: 117849.

62. Noam S, Evren Ö, Basser PJ, Yoram C. Accurate noninvasive measurement of cell size and compartment shape anisotropy in yeast cells using double-pulsed field gradient MR. *NMR Biomed.* 2012;25:236-246.

63. Henriques RN, Palombo M, Jespersen SN, Shemesh N, Lundell H, Ianus A. Double diffusion encoding and applications for biomedical imaging. *J Neurosci Methods.* 2021;348:108989.

SUPPORTING INFORMATION

Additional supporting information may be found in the online version of the article at the publisher's website.

Figure S1. BALL&Sphere impermeable - Signal fitting. The plots show the fitting of the BALL&Sphere model to the simulated signals with the diffusion time for different *b* (symbols), permeability (color) and cell size (columns).

Figure S2. CEXI - Signal fitting. The plots show the fitting of the CEXI model to the simulated signals with the diffusion time for different *b* (symbols), permeability (color) and cell size (columns).

Figure S3. Model estimates. The plots show the estimates of the Ball & Sphere (A-D) and CEXI (E-H) models from 30 DW-MRI signals with a SNR of 30.

Figure S4. BIC of model estimates. BIC of the impermeable Ball & Sphere model and CEXI for with increasing permeability, at different SNR.

Figure S5. Ball & Sphere estimates - Low ICVF - Noiseless. The plots show the estimates of the Ball & Sphere model in substrates with an ICVF of 0.2 from on noiseless signals.

Figure S6. Ball & Sphere estimates - Low ICVF - Noisy. The plots show the estimates of the Ball & Sphere model in substrates with an ICVF of 0.2 from 30 DW-MRI signals with a SNR of 30.

Figure S7. CEXI estimates - Low ICVF - Noiseless. The plots show the estimates of the CEXI model in substrates with an ICVF of 0.2 from on noiseless signals.

Figure S8. CEXI estimates - Low ICVF - Noisy. The plots show the estimates of the CEXI model in substrates with an ICVF of 0.2 from 30 DW-MRI signals with a SNR of 30.